Erosion Mechanism of the Gas-Solid Two-Phase Flow in Surface Pipelines for Shale Gas in the Sichuan Basin

Shaoquan Huo , Lincai Peng * , Yunpeng Li , Yong Xu , Hongbing Huang , Xi Yuan

Posted Date: 12 July 2024

doi: 10.20944/preprints202407.1067.v1

Keywords: shale gas; surface pipeline; L360N; erosion; surface protection

Article

Erosion Mechanism of the Gas, Solid Two, Phase Flow in Surface Pipelines for Shale Gas in the Sichuan Basin

Shaoquan Huo [1], Lincai Peng [1,*], Yunpeng Li [2], Yong Xu [3], Hongbing Huang [1] and Xi Yuan [1]

[1] Research Institute of Natural Gas Technology, PetroChina Southwest Oil and Gasfield Company, Chengdu, Sichuan, China; huoshq@petrochina.com.cn (S.H.); huanghb@petrochina.com.cn (H.H.); yuanxi@petrochina.com.cn (X.Y.)
[2] Chengdu Natural Gas Chemical Plant, PetroChina Southwest Oil and Gas Field Company, Chengdu, Sichuan, China; liyunpeng2019@petrochina.com.cn
[3] PetroChina Southwest Oil and Gasfield Company, Chengdu, Sichuan, China; xxyy@petrochina.com.cn
* Correspondence: lincai.peng@foxmail.com

Abstract: The erosion of surface pipelines induced by proppant flowback during shale gas production is significant. The surface pipelines in a shale gas field in the Sichuan Basin experienced perforation failures after only five months of service. To investigate the erosion features of L360N, coatings, and ceramics and optimize the selection of two protective materials, a gas,solid two,phase flow jet erosion experimental device was used to explore the erosion resistance of L360N, coating, and ceramic under different impact velocities (15 m/s, 20 m/s, and 30 m/s). An energy dispersive spectroscope, a scanning electron microscope, and a laser confocal microscope were employed to analyze erosion morphologies. With the increase in flow velocity, erosion depth and erosion rate of L360N, coating, and ceramic increased and peaked under an impact velocity of 30 m/s. Maximum erosion rate and maximum erosion depth of L360N were respectively 0.0350 mg/g and 37.5365 μm. Its primary material removal mechanism was plowing of solid particles and microcracks were distributed on the material surface under high flow velocities. Maximum erosion rate and maximum erosion depth of coating were respectively 0.0217 mg/g and 18.9964 μm. Its primary material removal mechanism was the detachment of the binder phase Co caused by plowing. Maximum erosion rate and maximum erosion depth of ceramics were respectively 0.0108 mg/g and 12.4856 μm. The erosion mechanisms were micro,cutting and plowing. Under different particle impact velocity, different erosion morphologies were observed, but the primary erosion mechanism was the same. The erosion resistance of ceramics was higher than that of coating. Therefore, ceramic lining materials could be used to protect the easily eroded parts, such as pipeline bends and tees, and reduce the failure rate by more than 93%. The study provided the data and theoretical basis for the theoretical study on oil and gas pipeline erosion and pipeline material selection.

Keywords: shale gas; surface pipeline; L360N; erosion; surface protection

1. Introduction

Shale gas resources in China rank first in the world and the total reserves are more than 2,000 trillion m^3 and widely distributed in the Sichuan Basin, the Ordos Basin, and other regions [1]. The large,scale hydraulic fracturing technology is applied in the development of shale gas and has improved mining efficiency and gas production, but it has also brought out a large number of problems caused by proppant flowback [1. In the exploitation and transportation process of shale gas, after desanding, the high,viscosity and high,stability fracturing flowback fluid still contains about 10% of sand particles before entering pipelines, thus causing pipeline erosion and wear [4,5], which seriously affect the flowback efficiency and the safety of shale gas exploitation.

The erosion process of shale gas pipelines under a gas,solid two,phase flow or a multi,phase flow is complex. Such flows are more prone to lead to sudden changes in flow patterns at some locations such as elbows, tee joints, and valves. The instantaneous impact velocity of the fluid is large and solid particles repeatedly collide with the inner wall of pipelines, thus leading to safety incidents

 doi:10.20944/preprints202407.1067.v1

such as wall thinning, perforation, and even damage and leakage of pipeline[6,7]. The erosion of surface pipelines in shale gas fields are affected by many factors, including the characteristics of target material, shape, particle size, hardness, impact velocity, impact angle, and flow characteristics[5,6,8,12]. The erosion mechanism of shale gas pipelines has been extensively explored at home and abroad. Liu et al. [11] analyzed the erosion mechanism of elbows in the Changning Shale Gas Field under different impact angles and indicated that the erosion rate and erosion area of elbows were mainly influenced by gas flow velocity and particle aggregation based on FLUENT simulation. With a two,way coupled Euler,Lagrange method in computational fluid dynamics (CFD) and response surface methodology (RSM), Chi et al. [4] investigated the factors of elbow erosion in shale gas gathering and transportation systems and found that the maximum erosion rate was positively correlated with bending angle, bending direction, particle size, particle velocity, and particle mass flow rate and negatively correlated with the inner diameter and R/D ratio of pipelines. Furthermore, the maximum erosion rate was influenced by the interaction of any two factors. Jia et al. [13] constructed a numerical model in FLUENT to explore the synergistic process of erosion and corrosion of 90° elbows in shale gas pipelines under gas,liquid,solid multi,phase flow conditions. Zhu et al. [14] studied the effects of inlet velocity, curvature diameter ratio, and pipe diameter on the erosion rate of 90° elbows through numerical simulations based on FSI,CFD and DPM. The previous studies on the erosion induced by proppant flowback during the production process of oil and gas wells mainly focused on numerical simulation [15,17]. However, the experimental studies on the gas,solid erosion damage in shale gas gathering and transportation pipelines, or the influences of various environmental factors on pipeline material erosion damage were seldom reported.

Proppant flowback caused by the large,scale hydraulic fracturing technology poses a serious erosion threat to pipelines. Therefore, it is significant to select appropriate protective materials and optimize material surface properties in the long,term service of shale gas pipelines. To address the problem of erosion in surface pipelines induced by proppants in shale gas gathering and transportation systems, surface treatment technologies such as electroplating, anodic oxidation, and ion implantation are increasingly applied in the protection of pipelines and equipment [18,19]. In recent years, high,hardness materials such as tungsten carbide cemented carbide and ceramics have attracted wide attention from the fields of materials science and petroleum engineering. These materials possess significant advantages in hardness, wear resistance, high,temperature resistance, and corrosion resistance for pipeline protection [20,26].

Surface pipelines in a shale gas field in the Sichuan Basin were made of L360N steel. After five months of service, one perforation occurred at the elbows of drainage pipelines and another perforation emerged three days after repair welding. The eroded hole was 4 cm long and 2 cm wide. The connecting pipe from the wellhead to the desanding skid failed after two months of service and an erosion depth was 3 to 4 mm. Metal coating or ceramic would be selected as protective materials for pipelines. Taking L360N steel, coatings, and ceramics as research objects, a gas,solid two,phase flow jet erosion experiment was conducted with a high,speed gas,sand jet erosion tester in order to explore the erosion patterns and mechanisms of L360N steel, coatings, and ceramics under different impact velocities at an impact angle of 30° in the study. Based on the experimental results, the protective material was selected from coatings and ceramics. The study provided the data and theoretical basis for the erosion theory research, engineering applications, and material selection of oil and gas pipelines.

2. Experiments

2.1. Materials

The materials used in the experiment were L360N, ceramics, and coatings. According to ASTM,G76 standard [27], the materials were cut into the specimens with the dimensions of 20×20×5 mm. A spark source atomic emission spectrometer was used to analyze the chemical composition of the three materials (Tables S1, S2, and S3). Before the experiment, the specimens were polished with sandpaper. A Huayin HVS,1000 Vickers hardness tester was used to measure the Vickers hardness

 doi:10.20944/preprints202407.1067.v1

of materials. To minimize measurement errors and calculate the average, Vickers hardness was measured at five locations on the specimen surface (Table 1) and the applied load during the experiment was 1000 gf. The average hardness of L360N, ceramics, and coating respectively reached 231.29 HV, 1644.57HV, and 1071.46 HV. Among the three materials, ceramic exhibited the highest hardness, followed by coating, and L360N had the lowest hardness. It is generally believed that the material with the higher hardness has the better erosion resistance [28].

Table 1. Vickers hardness of three materials.

Materials	**Vickers hardness (HV)**					
	Test 1	**Test 2**	**Test 3**	**Test 4**	**Test 5**	**Means**
L360N	220.72	225.97	202.39	267.57	239.79	231.29
Ceramic	1749.18	1702.85	1649.44	1468.97	1652.39	1644.57
Coating	1071.58	1065.48	1121.95	1062.54	1035.78	1071.46

According to ASTM,G76 standard, quartz sand was selected as the erosion particle. The particle size of quartz sand was determined with a Master sizer 2000 laser particle size analyzer (Figure S1). The particle size of quartz sand ranged from 20 μm to 126 μm with an average particle size of 48.479 μm. The size of 90% of particles was between 20 μm and 80 μm. The above data met the requirement for a median particle size of 50 μm in ASTM,G76 standard. The microscopic morphology of quartz sand is shown in Figure S2. Macroscopically, quartz sand appeared as white powder with irregularly shapes of different sizes. It had distinct edges and sharp corners and could simulate the erosion and wear of sand particles on pipelines and protective coatings during shale gas extraction, drainage, and production. Before each experiment, quartz sand was dried in an oven at 150 ℃ for 2 hours to ensure that particles in the sand,carrying fluid were in a dry state.

2.2. Method

2.2.1. Experimental Device

In this experiment, the AIR JET EROSION TESTER TR,470 model specified in ASTM,G76 standard was selected to carry out gas,solid two,phase jet erosion tests on L360N, ceramic, and coating under different flow velocities at normal temperature. As shown in Figure 1 [29], the experimental device is composed of an air jet erosion test bench, a piston air compressor, and a refrigeration dryer. The specimen was placed below the nozzle and the impact angle of the specimen could be changed through the specimen holder (Figure 1). The distance between the nozzle and the specimen surface was 10 mm and the nozzle diameter was 1.5 mm. During the solid particle erosion process, air was pressurized in the piston air compressor and then the moisture in the air flow was removed with the freeze dryer. Then, air was mixed evenly with the particles flowing out of the sand storage tank and accelerated within the reducing tube. Finally, air and particles impacted the target material at a constant speed, thus causing the mass loss of specimen materials.

Preprints.org (www.preprints.org) | NOT PEER-REVIEWED | Posted: 12 July 2024 doi:10.20944/preprints202407.1067.v1

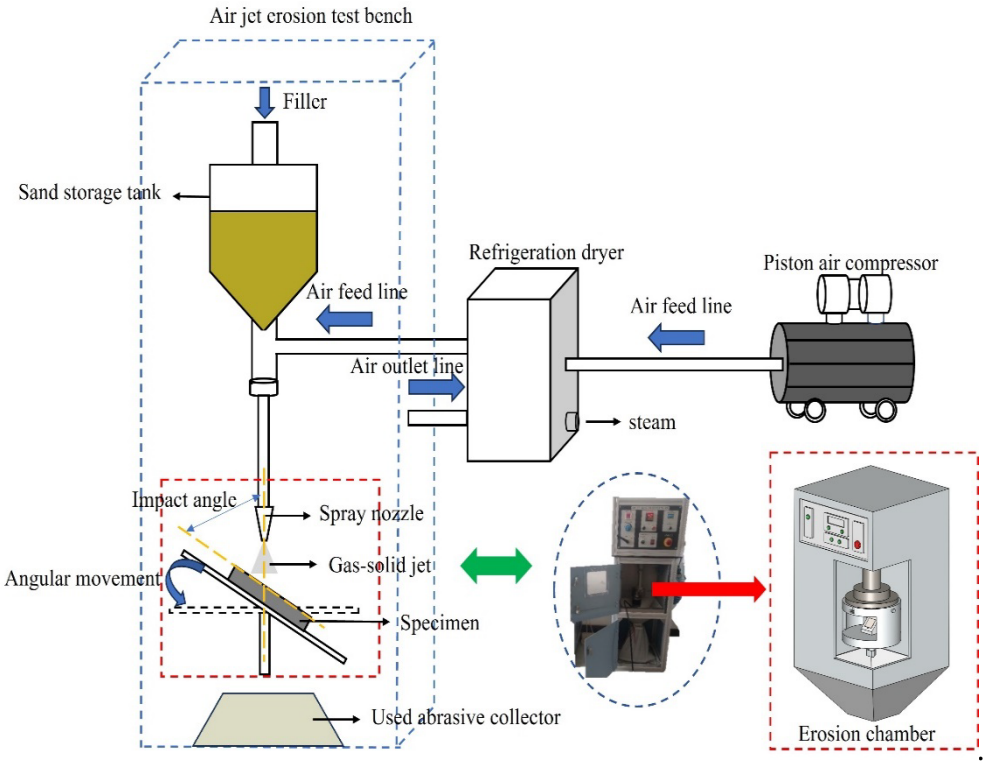

Figure 1. Experimental device for jet erosion tests of a gas,solid two,phase flow.

2.2.2. Measurement Method

The particle impact velocity was not equivalent to the gas flow velocity, so the double,disk method was adopted to measure the particle impact velocity under different inlet air pressures with measurement accuracy of ±2 m/s. The particle impact velocity was calculated with Eq. (1). The relationship between inlet air pressure and particle impact velocity is shown in Figure 2 [27]. In this experiment, the weight loss method was used to investigate the erosion features of specimens. The erosion rate of specimens was calculated with the ratio of the mass loss of specimens after erosion to the mass of solid particles used during the erosion process (Eq. (2)) [30].

$$V = H \times (N/60) \times (360/A) \quad (1)$$

where V indicates particle impact velocity (m/s); H indicates the distance between the upper and lower disks (m); N indicates the rotation speed of the motor (krpm); A indicates the mean of the measured angle (°).

$$E = 1000 \times (M_2 - M_1)/(Q_m \times t) \quad (2)$$

where E indicates erosion rate (mg/g); M_2 indicates the mass of the specimen after testing (g); M_1 indicates the mass of the specimen before testing (g); Q_m indicates mass flow rate of particles (g/min); t indicates erosion time (min).

To reduce experimental errors caused by surface roughness, before testing, the specimens were gradually polished with different waterproof sandpaper (Grit 600, Grit 800, Grit 1000, Grit 1200, and Grit 2000) and then polished. After rinsing with tap water, dehydrating with alcohol, and drying with cold air, the specimens were weighed with an electronic balance (accuracy = 0.1 mg). After the experiment, the residual quartz sand on the specimen surface was removed with anhydrous ethanol to weigh the specimen again and calculate the mass loss of specimens after erosion. The micro,morphology and chemical composition of the eroded area were analyzed with an FEI Quanta450 scanning electron microscope (SEM) and an energy dispersive spectrometer (EDS) at an acceleration voltage of 20 kV. A laser confocal microscope was used to observe the three,dimensional morphology and erosion depth of the eroded area. The local erosion rate was calculated to explore the erosion mechanism.

 doi:10.20944/preprints202407.1067.v1

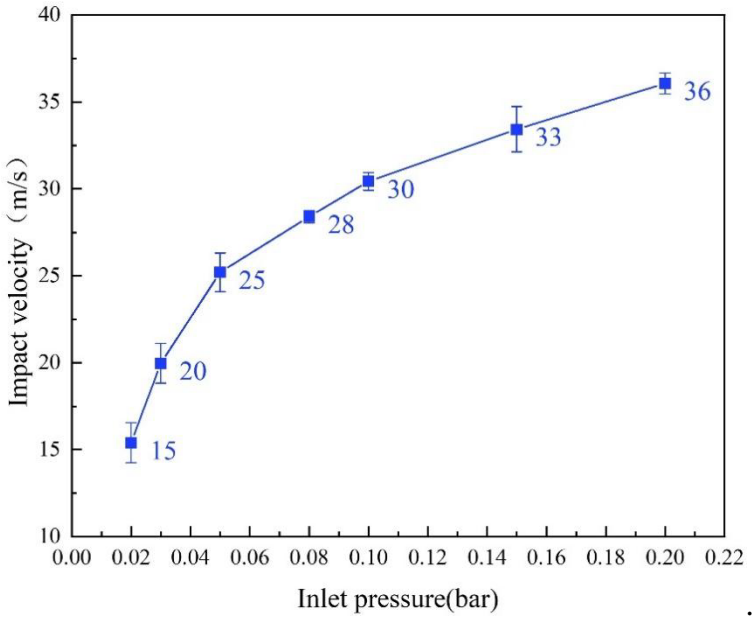

Figure 2. Relationship between inlet pressure and particle impact velocity.

2.2.3. Experimental Scheme

A gas,solid two,phase flow jet erosion experiment was conducted with L360N, coatings, and ceramics under simulated working conditions with an impact angle of 30° and impact velocities of 15 m/s, 20 m/s, and 30 m/s. The experiment was carried out under normal temperature and pressure. Erosion time for each specimen was 20 min and the mass flow rate of particles was 2 g/min. Five parallel specimens were set for each testing condition so as to ensure the accuracy and stability of experimental results. The experimental parameters are shown in Table 2.

Table 2. Experimental scheme of jet erosion under a gas,solid two,phase flow.

Experimental parameters	Setting
Erodent	Quartz sand
materials	L360N, Ceramic, Coating
Impact velocity (m/s)	15, 20, and 30
Experimental temperature (℃)	Room temperature
Impact Angle (°)	30
Particle mass flow (g/min)	2
Test duration (min)	20

3. Results and Discussion

3.1. Macroscopic Morphology Analysis

The macro,morphologies of L360N, ceramic, and coating under different impact velocities are shown in Figure 3. Under low erosion angles and different flow velocities, the erosion area gradually increased with the increase in impact velocity. The erosion area was the smallest under an impact velocity of 15 m/s and the largest under an impact velocity of 30 m/s. The erosion area showed significant differences among different materials and the erosion area of L360N was much larger than that of ceramics and coatings. After erosion, the eroded area appeared as a cone with a larger upper part and a smaller lower part and the cone opening formed an elongated irregular ellipse. According to the degree of erosion damage on the specimen surface, the erosion area could be divided into three parts: the elliptical central part with the highest degree of erosion (Part 1), the elliptical transition part with moderate erosion (Part 2), and the elliptical boundary area with slight erosion and lighter color (Part 3). In addition, the projected area of the nozzle was smaller than the erosion area (Figure 3). The

 doi:10.20944/preprints202407.1067.v1

contour of the upper erosion area of the test piece highly overlapped with the contour of the nozzle projection, but the lower erosion area of the test piece was much larger than the nozzle projection area. The difference might be interpreted as follows. Particles exhibited a higher degree of divergence under the erosion conditions of a small impact angle and were scattered over a larger area on the specimen surface, thus forming elliptical erosion pits during the impact process[31].

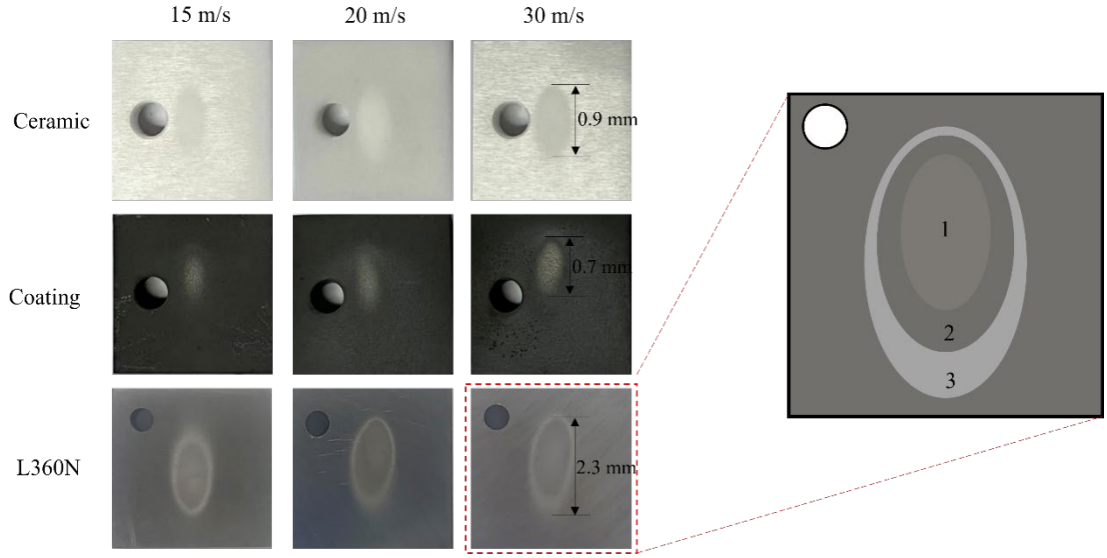

Figure 3. Macroscopic morphologies of L360N, ceramics, and coating under different impact velocities.

3.2. Influence of Impact Velocity on Erosion Rate

Figure 4 shows the erosion rates of L360N, ceramic, and coating after erosion for 20 min under impact velocities of 15 m/s, 20 m/s, and 30 m/s. The erosion rates of different materials increased with the increase in impact velocity, as reported by Modi et al. [32]. During the erosion process of solid particles, the particles flowing out of the sand storage tank initially had a velocity of zero. An air compressor provided pressurized air to accelerate solid particles, so that the sand,carrying fluid was ultimately ejected from the nozzle at a constant impact velocity to hit the target material. In this erosion process, particles acquired the kinetic energy from pressurized air. When the target material was impacted, the friction and collisions between particles and material molecules caused the material to deform, thus altering the relative positions between atoms, rearranging or breaking chemical bonds, and promoting the detachment of the material. Therefore, in order to increase the impact velocity of solid particles, it was necessary to increase the inlet air pressure. An increase in the kinetic energy gained by the particles was from the pressurized air. In this way, the material erosion was enhanced, thus leading to an increase in the erosion rate.

 doi:10.20944/preprints202407.1067.v1

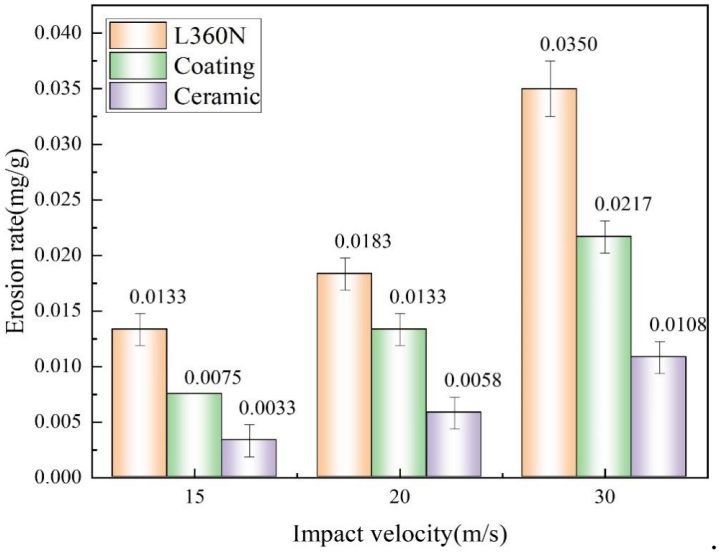

Figure 4. Erosion rates of L360N, ceramics, and coating under different impact velocities.

Under an impact velocity of 30 m/s, maximum erosion rates of L360N, coating, and ceramic were respectively 0.0350 mg/g, 0.0217 mg/g, and 0.0108 mg/g. The erosion rate of L360N was approximately 1.6 times higher than that of coating and 3.2 times higher than that of ceramic. Under the same impact velocity, the erosion rates of both ceramic and coating were significantly lower than that of L360N. The difference was ascribed to the differences in material properties. The erosion rate was greatly influenced by the hardness of materials. The material with higher hardness exhibited the stronger local resistance to the indentation of hard objects on their surfaces. Bhosale et al.[24] also reported that the high hardness of tungsten carbide,based coatings makes its erosion resistance superior to that of the steel substrate . Therefore, with the lowest hardness, L360N had the worst resistance to solid particle erosion, thus resulting in the largest mass loss caused by solid particles. In comparison, the ceramic had the highest hardness and demonstrated the higher erosion resistance.

3.3. 3D Surface Profiles

In order to further observe the micro,morphology of the erosion area and accurately measure the erosion depth of specimens, a laser confocal microscope was employed to observe the erosion trajectories of L360N, coating, and ceramic. The three,dimensional profiles of the eroded surfaces of L360N, coating, and ceramic after erosion are shown in Figure 5. In the central region of erosion pits, the three,dimensional profile morphologies of eroded surfaces were completely different among three materials and peaks and valleys were formed on material surfaces due to the different movement directions of solid particles during the erosion process. Especially, the coating surface exhibited obvious impact traces caused by small particles, thus resulting in an uneven erosion morphology with deeper erosion depths in local areas and uneven distributed erosion pits. SEM and EDS analysis results of the coating under different impact velocities indicated that the distribution of Co and WC particles of the binder phase in the coating was uneven. In the early erosion stage, due to the continuous impact of the sand,carrying fluid, the binder phase Co deformed and was detached firstly. During prolonged erosion, a few exposed WC particles were detached and pits were formed. The contents of Cr, Co, and W elements on the coating surface decreased after erosion, thus resulting in an uneven hill,like erosion morphology. Due to the high hardness of the ceramic, the impact of particles on the specimen was relatively small and strip,shaped processing traces could be observed on the ceramic surface under the low impact velocity. The cross,sectional profiles of the specimen were obtained along the surface,erosion pit,surface in the erosion damage area (Figure 6). The cross,sectional profiles of L360N and ceramic were V,shaped and maximum erosion depths of L360N and ceramic were 37.5365 μm and 12.4856 μm in the central region, respectively. The erosion pits on

 doi:10.20944/preprints202407.1067.v1

coating surface were more than those on L360N surface and maximum erosion depth on coating surface was 18.9964 μm.

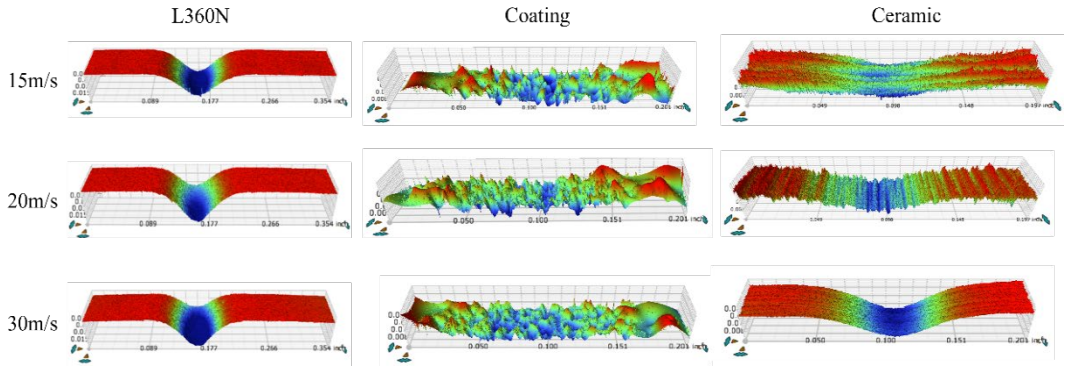

Figure 5. Erosion morphologies of L360N, ceramic, and coating under a confocal microscope.

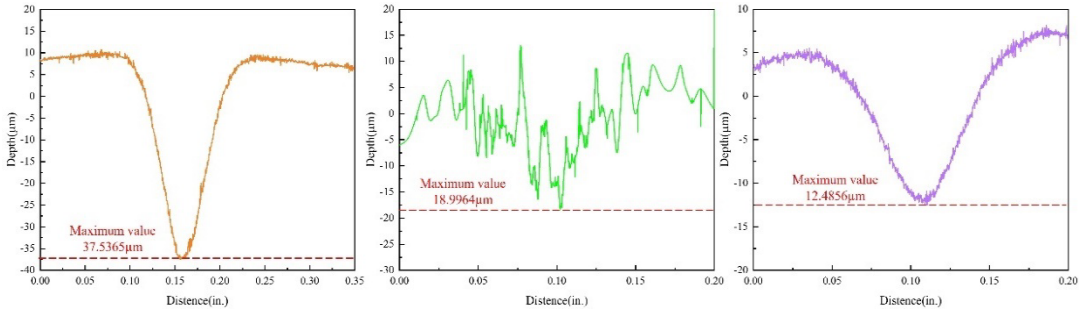

Figure 6. Section outlines of the three materials under an impact speed of 30 m/s: (a) L360N, (b) coating, and (c) ceramic.

The erosion depths of the specimens under different impact velocities are shown in Table 3. With the increase in particle impact velocity, the impact energy also gradually increased. Solid particles exhibited higher velocity and kinetic energy under an impact velocity of 30 m/s, thus resulting in deeper and larger erosion pits compared to those under an impact velocity of 15 m/s. The result of erosion depth was well consistent with the pattern of erosion rate.

Table 3. Erosion depth of specimens under different impact velocities.

Materials	L360N	Coating	Ceramic
Impact velocity (m/s)		Maximum erosion depths (μm)	
15	13.6494	10.6588	2.4304
20	18.5994	14.6526	3.9132
30	37.5365	18.9964	12.4856

To more accurately compare the erosion conditions of specimens under different impact velocities, the local erosion rate were calculated with erosion depth (Eq. (3)). The maximum depth measured under a confocal microscope was determined as the erosion depth.

$$E_D = h / t \tag{3}$$

where E_D indicates local erosion rate (mm/d); h indicates erosion depth (mm); t indicates erosion time (days).

 doi:10.20944/preprints202407.1067.v1

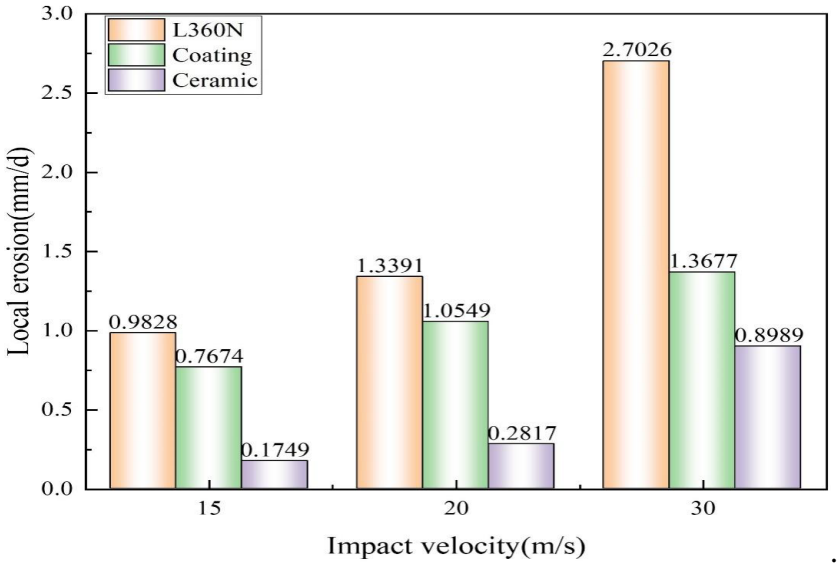

Figure 7. Local erosion rates of L360N, coating, and ceramic under different impact velocities.

Local erosion rate gradually increased with the increase in impact velocity (Figure 7). Under the impact velocity of 30 m/s, local erosion rates of L360N, coating, and ceramic were 2.7026 mm/d, 1.3677 mm/d, and 0.8989 mm/d, respectively. In the shale gas production process, some parts such as elbows and tee joints were significantly affected by local erosion. In the high sand production stage of the drainage period, the thickness of the plug used in the shale gas gathering and transportation system was decreased by 43.73 mm in 20 days. In Changning Shale Gas Field, the annual erosion thickness of the desander exceeded 100 μm under a flow rate of 12 m/s. Therefore, it is necessary to take corresponding protective measures to mitigate the erosion. When the impact velocity was slower than 20 m/s, the growth trend of the local erosion rate of ceramic was relatively gentle and the local erosion rate of coating was about 3.7 times of that of ceramic. When the impact velocity exceeded 20 m/s, the growth trend of the local erosion rate of ceramic increased sharply and the growth trend of coating was less significant than that of ceramic. However, the local erosion rate of coating still exceeded that of ceramic. Under different impact velocities, the erosion resistance of high,hardness ceramic was better than that of coating. The erosion resistance of the three materials ranked in the following order: ceramic > coating > L360N.

3.4. Erosion Mechanism Analysis

Erosion is an extremely complex physical process. To investigate the erosion mechanisms of L360N, ceramic, and coating under different impact velocities, the microscopic morphology of the specimen surfaces was analyzed with FEI Quanta450 scanning electron microscope (SEM) at an accelerated voltage of 20 kV. The microscopic morphologies are shown in Figures 8, 9, and 10.

 doi:10.20944/preprints202407.1067.v1

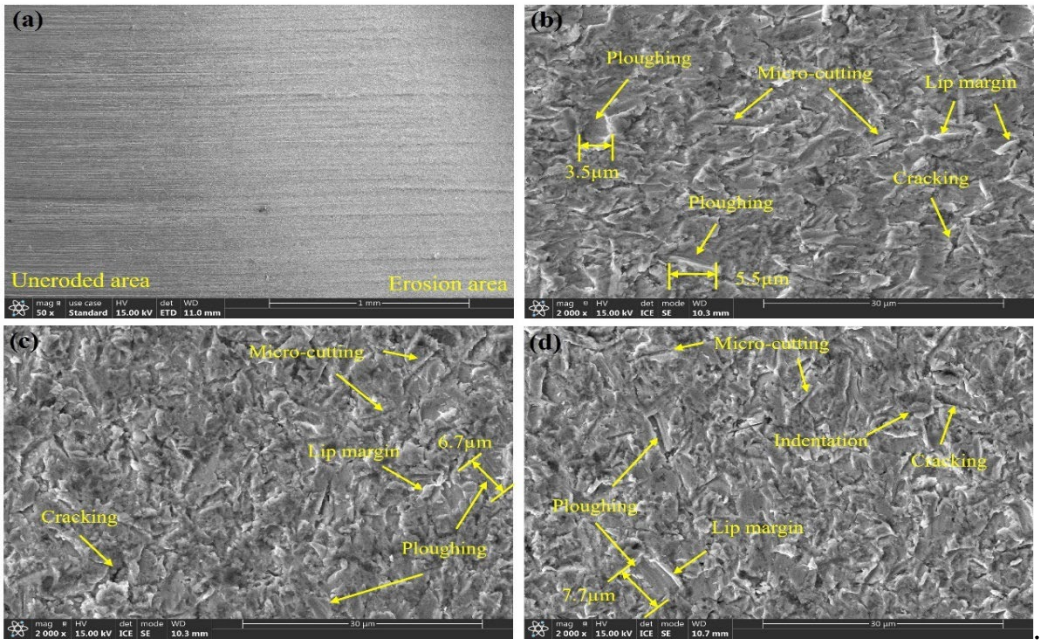

Figure 8. Micromorphologies of L360N under different impact velocities: (a) before and after erosion, (b) 15 m/s, (c) 20 m/s, and (d) 30 m/s.

The microstructures of L360N under different impact velocities are shown in Figure 8. The microstructures of L360N before and after erosion were compared. A large number of metal processing scratches were observed on the surface of the uneroded area. However, in the eroded area, the number of scratches was significantly decreased and the obvious trace of erosion transition was observed. The main mechanisms for material removal included plowing and micro,cutting as well as indentation (Figures 8(b), 8(c), and 8(d)). The surface of L360N exhibited wavy folds with a large number of overlapping and intersecting grooves, whose directions were consistent with the flow direction of the sand,carrying fluid. With the increase in impact velocity, the depth of plowing grooves increased from 3.5 μm to 7.7 μm and obvious protruding lips were observed on both sides and ends of the grooves. Their formation was mainly ascribed to the plastic deformation of materials caused by scraping, micro,cutting, and plowing effects of irregular solid particles carried by high,velocity gas [8,9]. In addition, a small number of microcracks could be observed on the material surface. The continuous impact and compression of quartz sand on the material surface hardened the material and enhanced its brittleness. When the uneven stress exceeded the material threshold, cracks were generated under the impact of subsequent particles [33,34].

The force analysis of specimens was performed under an impact angle of 30°. The specimen was subjected to a horizontal tangential force from the sand,carried fluid along its surface and a perpendicular pressure. Liu et al. [33] confirmed that the tangential force generated by erosion particles impacting the surface reached its maximum value at the lower angles between 15° and 30°. The tangential force caused by particle impact exerted a micro,cutting effect on L360N. Under this micro,cutting effect, the lips formed by plastic deformation of the material broke into debris and detached from the surface. As solid particles further impacted the surface, new lips were formed on the surface, thus leading to the continuous mass loss of L360N [35]. The pressure generated by particle impact exerted the impact and compression effect on the materials. Repeated compression and forging by the sand,carried fluid caused the indentation depth on the material surface to further increase. Therefore, the cutting effect of the horizontal component on the specimen surface and the impact and compression effect of the vertical component led to the repeated surface plastic deformation of L360N.

 doi:10.20944/preprints202407.1067.v1

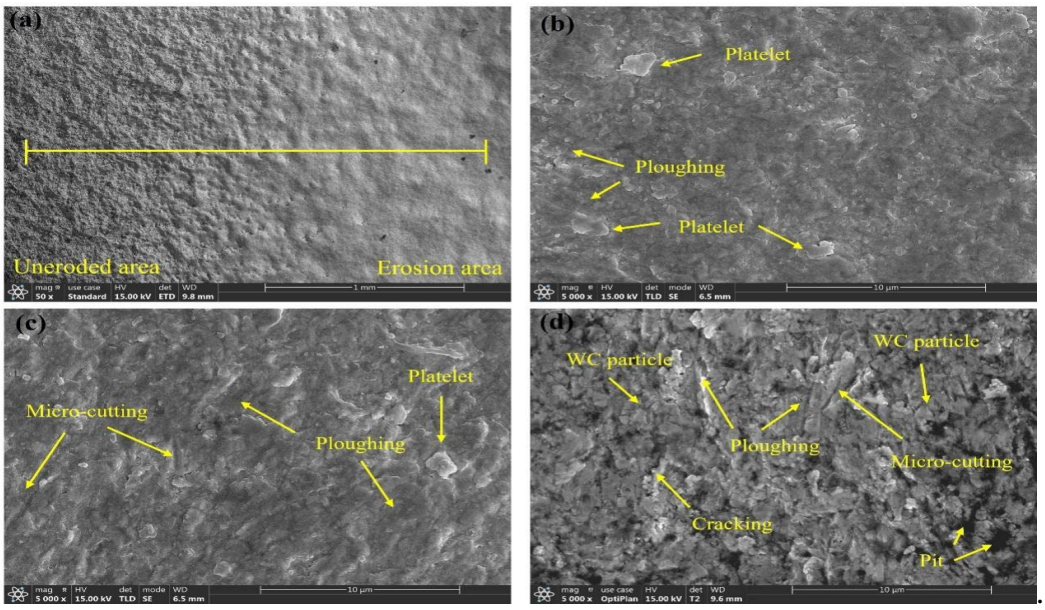

Figure 9. Microstructure of the coating under different impact velocities: (a) before and after erosion, (b) 15 m/s, (c) 20 m/s, and (d) 30 m/s.

The microscopic morphology of coating under different impact velocities is shown in Figure 9. The microscopic morphology of coating before and after erosion was compared. The surface of the non,eroded area was porous, loose, and full of holes, whereas the eroded and worn area was smooth but uneven. Under an impact angle of 30°, the main mechanisms of material removal included plowing and micro,cutting and a small amount of irregular flake residues remained on the surface (Figures 9(b), 9(c), and 9(d)). When the impact velocity increased to 30 m/s, small cracks and a few pits appeared on the coating surface and numerous protruding solid particles were distributed in a scattered pattern. It was speculated that the of WC and Co elements with different hardness were unevenly distributed on the coating surface and resulted in the difference in the degrees of erosion and wear during the erosion process and the uneven coating surface. To investigate the elemental distribution on the coating surface before and after erosion, an elemental line scan was performed on the eroded area according to the scanning direction from the matrix to the erosion pit. The results of the elemental line scan are shown in Figure 10. The main elements on the coating surface were C, Cr, Co, and W. As erosion depth gradually increased, the contents of Cr, Co, and W also gradually decreased and abruptly dropped at the depth of 1460 μm.

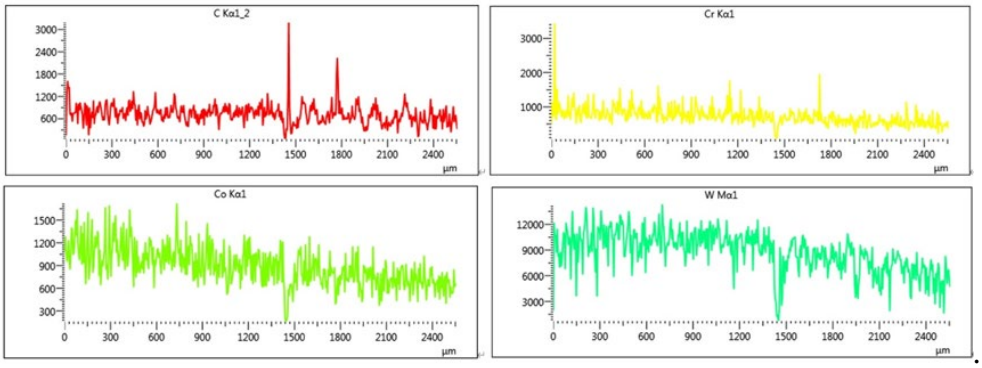

Figure 10. Elemental line scan result of the plating coating.

Based on SEM and EDS results, after the erosion, Co and WC particles of the binder phase on the coating surface were detached. Under an impact angle of 30°, the cutting effect of the horizontal component on the specimen surface outweighed the impact and compression effect of the vertical

 doi:10.20944/preprints202407.1067.v1

component. Additionally, the hardness of the binder phase Co in the coating was lower than that of WC particles. Quartz sand particles with small size and sharp edges would preferentially cause plastic deformation of the binder phase Co due to their cutting effect on the coating. Repeated impacts of quartz sand particles led to the formation of flakes and detachment of protruding lips (Figure 9(b)) [20]. With the increase in erosion time, WC particles lost the support of the binder phase and became exposed, so they were unevenly distributed on the coating surface (Figure 9(d)). At low angles, quartz sand particles with high impact energy and hardness further laterally impacted and cut protruding WC particles, thus resulting in cracking, detachment, and the formation of pits at a few locations [34,36]. In addition, a small number of microcracks were observed on the material surface. WC particles hindered the plastic deformation of the binder phase, so the mutual compression between them easily led to crack formation at boundaries. The decreased bonding strength between WC particles and the binder phase disrupted the stability of WC particles, thus causing their displacement under continuous impacts of solid particles [37]. The interaction between the plastic deformation of the binder phase Co and the displacement of WC particles led to the transverse expansion of cracks along boundaries, thus promoting the detachment of coating. It is generally believed that the high hardness of composite materials contributes to the resistance to deformation and displacement, but it is disadvantageous to the resistance the detachment of already deformed and displaced parts. Therefore, increasing the hardness of WC particles could significantly improve the erosion resistance of coating. As the hardness of WC particles was greater than that of quartz sand, under a small impact angle of 30°, the detachment of the binder phase Co caused by micro,cutting of quartz sand was mainly responsible for coating erosion and wear, Cracking and displacement of WC particles could reduce the erosion resistance of coating, enhance the cutting effect of solid particles on the coating, and further increase the mass loss of the material [20].

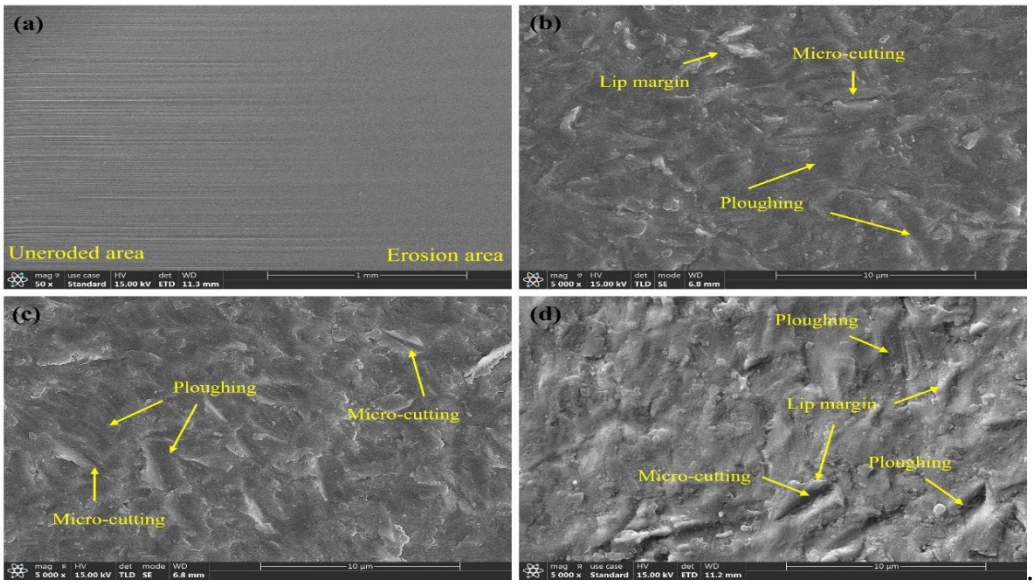

Figure 11. Micromorphology of ceramic under different impact velocities: (a) before and after erosion, (b) 15 m/s, (c) 20 m/s, and (d) 30 m/s.

The microscopic morphologies of ceramic under different impact velocities are shown in Figure 11. The microscopic surface morphologies of ceramic before and after erosion were compared. On the surface of the non,eroded area, a large number of machining scratches were observed, but the eroded and worn area had a smooth and flat surface. The ceramic surface was relatively smooth and flat. Only a small amount of plowing and micro,cutting traces were distributed and crack or pit was not observed (Figures 11(b), 11(c), and 11(d)). Under an impact angle of 30°, the mechanisms of material removal under different impact velocities were not different and included both plowing and micro,cutting. When the impact velocity was 15 m/s, the plastic deformation on the ceramic surface was relatively small and only a few protruding lips were observed. Under slow flow velocities, the

 doi:10.20944/preprints202407.1067.v1

horizontal component of kinetic energy was small and the hardness of ceramic exceeded than that of quartz sand, so the cutting effect of the fluid on ceramic was relatively weak. Under an impact speed of 30 m/s, the plastic deformation of ceramic surface was significantly enhanced. The cutting effect of the fluid on ceramic under a fast flow velocity led to deeper furrows on the material surface, and many thicker lips were observed. It is generally believed that the erosion rate of brittle materials is the highest under an impact angle of 90°, so the ceramic has the higher erosion resistance under an impact angle of 30° [39].

In summary, the erosion mechanisms of the three materials under different flow velocities are mainly micro,cutting and plowing. The surface of L360N showed cracking and indentation and the coating surface showed the detachment phenomenon of binder phase Co and WC particles. The ceramic surface remained intact without crack or pit. Under an impact angle of 30°, for the same material, even though the microscopic morphologies formed under different impact velocities showed significant differences, the mechanisms of material removal were almost the same, indicating that the changes in particle impact velocity did not affect the erosion mechanism. As the particle impact velocity increased, the length of furrows also increased, suggesting that an increase in impact velocity enhanced the impact energy and surface tangential force of solid particles. Therefore, micro,cutting and plowing caused more severe erosion and abrasion and the erosion rate increased. L360N exhibited the obvious characteristics of plastic material erosion and coating and ceramic showed the erosion behavior of brittle materials. Compared with L360N, coating and ceramic had the larger hardness, the better erosion resistance, and significantly higher resistance to plastic deformation under high impact velocities than L360N.

Figure 12 shows the influences of particle impact velocity on the erosion of three materials. The impact velocities of solid particles increase from top to bottom, i.e., $v_1 > v_2 > v_3$. When particle impact velocity is v_1, the kinetic energy acquired by solid particles from the sand,carrying fluid is relatively small. When solid particles strike the material at an impact angle of 30°, the horizontal component of kinetic energy causes plastic deformation of the material surface, leaving furrows along the cutting trajectory and extruding the material towards both sides and the front to form lips. Solid particles acquire less energy, so their energy is consumed after they travel a short distance on the material surface. Then, the cutting effect stops and shorter furrows are formed on the material surface. Additionally, due to the slower velocity, the impact of the sand,carrying fluid on lips is relatively weak and the lips formed on the material surface less are not easily eroded. Therefore, after continuous erosion, intersecting furrows and a large number of uneroded lips are eventually left on the material surface. When the particle impact velocity is v_2, the energy acquired by a single solid particle also increases. When a solid particle impacts the material surface at the same incident angle, the micro,cutting effect is stronger and long and deep furrows are formed on material surface. When the particle impact velocity is v_3, the overlapping and intersecting furrows are more pronounced and the erosion effect of the sand,carrying fluid on lips is also stronger under high flow velocities. The impact of the fluid can lead to the detachment of lips and increase the mass loss of the material as the flow velocity increases. When the non,uniform stress caused by impact and compression exceeds the material threshold, cracks are formed in the material.

 doi:10.20944/preprints202407.1067.v1

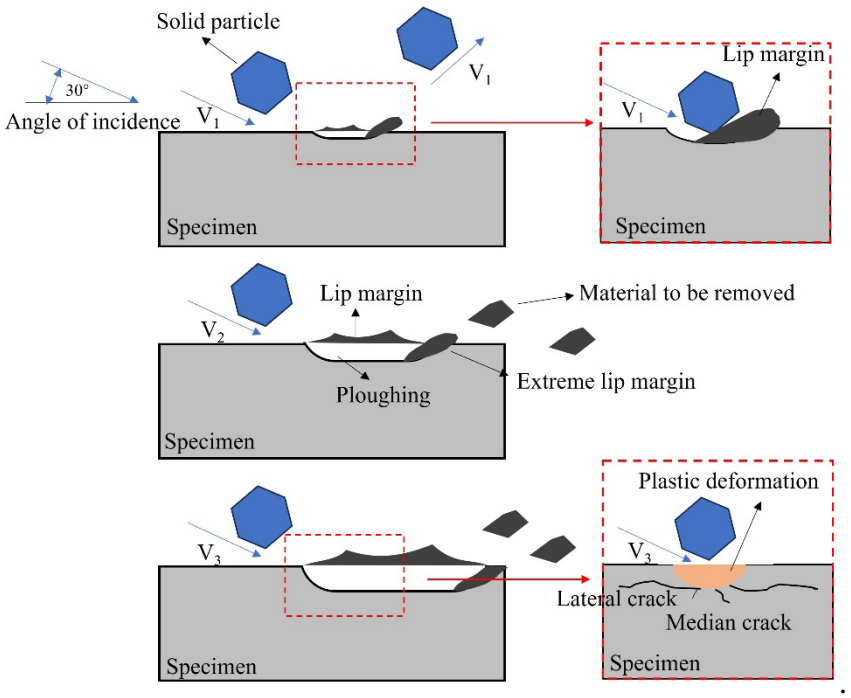

Figure 12. Schematic diagram of erosion mechanism under different impact velocities.

The experimental results showed that under any velocity, erosion rate, erosion depth, and local erosion rate of the high,hardness ceramic were all lower than those of coating. Under an impact velocity of 30 m/s, the erosion rate of coating was 2 times of that of ceramic and its local erosion rate was 1.5 times that of ceramic. Compared with ceramic, coating had the lower hardness and the weaker resistance to micro,cutting and plowing. Under a high impact velocity, pits and cracks appeared on the coating surface. The erosion resistance of ceramic was much better than that of coating. Therefore, ceramic lining materials were used to protect the easily eroded parts, such as pipeline bends and tees. Currently, erosion,resistant components such as zirconia ceramic,lined elbows and zirconia ceramic,lined three,way pipes have been applied in shale gas surface pipelines. The service life of these elbows has increased from 5 months to 2 years without any failure and no corrosion has been found in pipelines so far. Due to its excellent corrosion resistance and erosion resistance, ceramic played the significant protective role in shale gas surface pipelines. Additionally, thicker bends or square bends significantly reduced erosion and wear caused by proppant flowback and thus decreased the failure rate by 93%.

4. Conclusion

To solve the erosion problem caused by proppant flowback during shale gas production, a high,speed gas,sand jet erosion tester was used to conduct gas,solid two,phase jet erosion experiments with L360N, coating, and ceramic under simulated working conditions. The erosion wear performance of L360N, coating, and ceramic under the impact velocities of 15 m/s, 20 m/s, and 30 m/s was analyzed. The conclusions are drawn as follows:

(1) under an impact angle of 30°, erosion rate, erosion depth, and local erosion rate of L360N, coating, and ceramic increased with the increase in impact velocity. Under an impact velocity of 30 m/s, maximum erosion rates of L360N, coating, and ceramic were respectively 0.0350 mg/g, 0.0217 mg/g, and 0.0108 mg/g. Maximum erosion depths of L360N, coating, and ceramic were respectively 37.5365 μm, 18.9964 μm, and 12.4856 μm. Due to their high hardness, the erosion rates of coating and ceramic were seldom changed with the increase in impact velocity. Among the three materials, ceramic exhibited the best erosion resistance, whereas L360N had the worst erosion resistance.

(2) the erosion mechanisms of the three materials under different flow rates were primarily micro,cutting and plowing. Cracks and indentations appeared on the surface of L360N, whereas Co

and WC particles in the binder phase were detached from coating surface. The ceramic surface remained intact and crack or pit was not observed. For the same material, erosion morphology varied with particle impact velocity, but the change in particle impact velocity did not affect the primary erosion mechanism. Increasing the impact velocity increased impact energy and tangential force of solid particles on the surface, thereby increasing erosion rate.

(3) erosion rate, erosion depth, and local erosion rate of high,hardness ceramics were all smaller than those of coating. The erosion resistance of ceramics was much better than that of coating. Therefore, erosion,resistant components such as zirconia ceramic lined bends and zirconia ceramic lined tees were used to protect shale gas surface pipelines. After two years of service, no failure occurred and the erosion and wear problem of surface pipelines caused by proppant flowback was solved.

Author Contributions: Methodology, writing and editing, S.H.; conceptualization, validation and review, L.P.; validation and investigation, Y.L.; software and formal analysis, Y.X.; review and editing, H.H.; supervision and validation, X.Y. All authors have read and agreed to the published version of the manuscript.

Institutional Review Board Statement: Not applicable.

Informed Consent Statement: Not applicable.

Data Availability Statement: Data is unavailable due to privacy restrictions.

Conflicts of Interest: The authors declare no conflict of interest.

Reference

1. Wu, G.Y.; Zhao, W.W.; Wang, Y.R.; Tang, Y.F.; Xie, M. Analysis on corrosion,induced failure of shale gas gathering pipelines in the southern Sichuan Basin of China[J]. *Eng. Fail. Anal*. **2021**, 130, 105796. doi.org/10.1016/j.engfailanal.2021.105796.
2. K.B.Gregory; R.D.Vidic; D.A.Dzombak. Water management challenges associated with the production of shale gas by hydraulic fracturing[J]. *Elements*. **2011**, 7, 181,186. doi.org/10.2113/gselements.7.3.181.
3. Zeng, D.; Zhang, S.; Li, J.; Wang, X.; Tian, G.; Zhang, X.; Yu , H.Y.; Li, X.G. [J]. Wear. 2023, 528, 204980. doi.org/10.1016/j.wear.2023.204980.
4. Chi, M.H.; Zeng, X.G.; Gao, Y.P.; Li, W.; Jiang, H.Y.; Sun, R.C. The erosion rate prediction for the elbow in shale gas gathering and transportation system: RSM and GA,BP,ANN modeling[J]. *Powder. Technol*. **2024**, 435, 119429. doi.org/10.1016/j.powtec.2024.119429.
5. M.Parsi; K.Najmi; F.Najafifard; S.Hassani; B.S.McLaury; S.A.Shirazi. A comprehensive review of solid particle erosion modeling for oil and gas wells and pipelines applications[J]. *J Nat. Gas. Sci. Eng*. **2014**, 21, 850,873. doi.org/10.1016/j.jngse.2014.10.001.
6. Hong, B.Y.; Li, Y.B.; Li, Y.; Gong, J.; Yu, Y.F.; Huang, A.D.; Li, X.P. Numerical simulation of solid particle erosion in the gas,liquid flow of key pipe fittings in shale gas fields[J]. *Case. Stud. Therm. Eng*. **2023**, 42, 102742. doi.org/10.1016/j.csite.2023.102742.
7. Hong, B.Y.; Li, X.P.; Li, Y.B.; Li, Y.; Yu, Y.F.; Wang Y.M.; G, J.; A, D.H. Numerical simulation of elbow erosion in shale gas fields under gas,solid two,phase flow[J]. *Energies*. **2021**, 14, 3804. doi.org/10.3390/en14133804.
8. Hong, B.Y.; Li, Y.B.; Li, X.P.; Li, G.; Huang, O.; Ji, S.P.; Li, W.D.; G, J.; Guo, J. Experimental investigation of erosion rate for gas,solid two,phase flow in 304 stainless/L245 carbon steel[J]. *Petrol. Sci.* **2022**, 19, 1347,1360. doi.org/10.1016/j.petsci.2022.01.011.
9. M.Vite,Torres; J.R.Laguna,Camacho; R.E.Baldenebro,Castillo; E.A.Gallardo,Hernández; E.E.Vera,Cárdenas; J.Vite,Torres. Study of solid particle erosion on AISI 420 stainless steel using angular silicon carbide and steel round grit particles[J]. *Wear*. **2013**, 301, 383,389. doi.org/10.1016/j.wear.2013.01.071.
10. P.S.Babu; B.Basu; G.Sundararajan. The influence of erodent hardness on the erosion behavior of detonation sprayed WC,12Co coatings[J]. *Wear*. **2011**, 270, 903,913. doi.org/10.1016/j.wear.2011.02.019.
11. Liu, E.B.; Huang, S.; Tian D.C.; Shi, L.M.; Peng, S.B.; Zheng, H. Experimental and numerical simulation study on the erosion behavior of the elbow of gathering pipeline in shale gas field[J]. *Petrol. Sci*. **2024**, 21, 1257,1274. doi.org/10.1016/j.petsci.2023.08.034.
12. J.Zaragoza,Granados; E.A.Gallardo,Hernandez; M.Vite,Torres; C.Sedano,de la Rosa. Erosion behaviour of AISI 310 stainless steel at 450 C under turbulent swirling impinging jets[J]. *Wear*. **2019**, 426, 637,642. doi.org/10.1016/j.wear.2019.01.076.

13. Jia, W.L.; Zhang, Y.R.; Li, C.J.; Luo, P.; Song, X.Q.; Wang, Y.Z.; Hu, X.Y. Experimental and numerical simulation of erosion,corrosion of 90 steel elbow in shale gas pipeline[J]. *J Nat. Gas. Sci. Eng*. **2021**, 89, 103871. doi.org/10.1016/j.jngse.2021.103871.
14. Zhu, H.J.; Zhao, H.N.; Pan, Q.; Li, X. Coupling analysis of fluid,structure interaction and flow erosion of gas,solid flow in elbow pipe[J]. *Adv. Mech. Eng*. **2014**, 2014, 815945. doi.org/10.1155/2014/815945.
15. Peng, W.S.; Cao, X.W.; Li, M.; Wang, P.; Bian, J.; Lin, C.G.. Sand erosion prediction models for two,phase flow pipe bends and their application in gas,liquid,solid multiphase flow erosion[J]. *Powder. Technol*. **2023**, 421, 118421. doi.org/10.1016/j.powtec.2023.118421.
16. Song, X.Q.; Luo, P.; Luo, S.Y.; Huang, S.W.; Wang, Z.L. Numerical simulation study on the influence of incident position on erosion characteristics of gas,particle two,phase flow in 90° elbow[J]. *Adv. Mech. Eng*. **2017**, 9, 1687814017733249. doi.org/10.1177/1687814017733249.
17. Zhang, E.B.; Zeng, D.Z.; Zhu, H.J.; Li, S.G.; Chen, D.B.; Ding, Y.Y.; Tian; G. Numerical simulation for erosion effects of three,phase flow containing sulfur particles on elbows in high sour gas fields[J]. *Petroleum*, **2018**, 4, 158,167. doi.org/10.1016/j.petlm.2017.12.008.
18. M.Ashokkumar; D.Thirumalaikumarasamy; P.Thirumal; R.Barathiraja. Influences of Mechanical, Corrosion, erosion and tribological performance of cold sprayed Coatings A review[J]. *Mater Today: Process*, **2021**, 46, 7581,7587. doi.org/10.1016/j.matpr.2021.01.664.
19. R.K.Sharma; R.K.Das; S.R.Kumar. Effect of chromium–titanium on corrosion and erosion of HVOF coating[J]. *Surf. Eng*. **2022**, 38, 366,374. doi.org/10.1080/02670844.2022.2076015.
20. M.A.González; E.Rodríguez; E.Mojardín; O.Jiménez; H.Guillen; J.Ibarra. Study of the erosive wear behaviour of cryogenically and tempered WC,CoCr coating deposited by HVOF[J]. *Wear*. **2017**, 376, 595,607. doi.org/10.1016/j.wear.2016.12.061.
21. Geng, Z., Hou, S., Shi, G., Duan, D., & Li, S.. Tribological behaviour at various temperatures of WC,Co coatings prepared using different thermal spraying techniques. *Tribol Int*. **2016**, 104: 36,44. https://doi.org/10.1016/j.triboint.2016.08.025.
22. Bolelli, G., Berger, L. M., Börner, T., Koivuluoto, H., Matikainen, V., Lusvarghi, L., Vuoristo, P.. Sliding and abrasive wear behaviour of HVOF,and HVAF,sprayed Cr_3C_2–NiCr hardmetal coatings. *Wear*. **2016**, 358: 32,50. https://doi.org/10.1016/j.wear.2016.03.034.
23. Ćurković, L., Landek, D., Švagelj, Z., Gabelica, I.. The volume erosion rate of the slip cast monolithic and composite ceramics. *Adv Appl Ceram*. **2023**, 122(3,4): 119,128. https://doi.org/10.1080/17436753.2023.2235491.
24. Bhosale, D. G., Prabhu, T. R., Rathod, W. S., Patil, M. A., & Rukhande, S. W.. High temperature solid particle erosion behaviour of SS 316L and thermal sprayed WC,Cr_3C_2–Ni coatings. *Wear*. **2020**, 462: 203520. https://doi.org/10.1016/j.wear.2020.203520.
25. de Portu, G., Pinasco, P., Melandri, C., Capiani, C., Guardamagna, C., Lorenzoni, L., & Cernuschi, F.. Solid particle erosion behavior of laminated ceramic structures. *Wear*. **2020**, 442: 203147. https://doi.org/10.1016/j.wear.2019.203147.
26. Medvedovski, E..Advanced ceramics and coatings for erosion-related applications in mineral and oil and gas production: A technical review. *Int J Appl Ceram Tec*. **2023**. 20(2): 612,659. https://doi.org/10.1111/ijac.14240.
27. ASTM,G76 standard，Standard Test Method for Conducting Erosion Tests by Solid Particle Impingement Using Gas Jets.
28. Verdi, D., Cortés, R., Chia, G. Y., & Tay, G.. Erosion behaviour of laser cladded Inconel 625,Vanadium carbide metal matrix composites coatings manufactured with different reinforcement contents. *Surf Coat Tech*. **2024**, 476: 130282. https://doi.org/10.1016/j.surfcoat.2023.130282.
29. Deng, K., Zhou, N., Lin, Y., Cheng, J., Bing, L., & Jing, Z..Experimental and numerical study on the high,speed gas,solid nozzle erosion of choke manifold material in high pressure and high production gas well. *Powder Technol*. **2024**, 438: 119628. https://doi.org/10.1016/j.powtec.2024.119628.
30. Erdoğan, A. A., Feyzullahoğlu, E., Fidan, S., Sinmazçelik, T.. Investigation of erosive wear behaviors of AA6082,T6 aluminum alloy. *P I Mech Eng L,J Mat*. **2020**, 234(3): 520,530. https://doi.org/10.1177/1464420719899686.
31. Laguna,Camacho, J. R., Marquina,Chávez, A., Mendez,Mendez, J. V., Vite,Torres, M., Gallardo,Hernandez, E. A.. Solid particle erosion of AISI 304, 316 and 420 stainless steels. *Wear*. 2013, 301(1,2): 398,405. https://doi.org/10.1016/j.wear.2012.12.047.
32. Modi, O. P., Prasad, B. K., Jha, A. K.. Influence of alumina dispersoid and test parameters on erosive wear behaviour of a cast zinc–aluminium alloy. *Wear*. **2006**, 260(7,8): 895,902. https://doi.org/10.1016/j.wear.2005.06.015.

 doi:10.20944/preprints202407.1067.v1

33. Liu, B., Liu,X., Deng, K., H., Lin, K., H. , Zhou, N., T., Mei, Z.,B., Li, S.,G.. Erosion Mechanism of 30CrMo Steel Impacted by High Speed Solid Particles. *Surf. Technol.* **2023**, 52(9): 135,145. https://doi.org/10.16490/j.cnki.issn.1001,3660.2023.09.010.
34. Ribu, D. C., Rajesh, R., Thirumalaikumarasamy, D., Kaladgi, A. R., Saleel, C. A., Nisar, K. S., Afzal, A.. Experimental investigation of erosion corrosion performance and slurry erosion mechanism of HVOF sprayed WC,10Co coatings using design of experiment approach. *J Mater Res Technol*. **2022**, 18: 293,314. https://doi.org/10.1016/j.jmrt.2022.01.134.
35. Zhao, Y. L., Tang, C. Y., Yao, J., Zeng, Z. H., Dong, S. G.. Investigation of erosion behavior of 304 stainless steel under solid–liquid jet flow impinging at 30. *Petrol Sci*. **2020**, 17: 1135,1150. https://doi.org/10.1007/s12182,020,00473,7.
36. Liu, L., Zhang, K., Wang, Y.. Baffle effect of exposed WC particles in the clearance on slurry erosion behavior of cemented carbide surface. *Mater Today Commun*. **2024**, 39: 109071. https://doi.org/10.1016/j.mtcomm.2024.109071.
37. Vashishtha, N., Khatirkar, R. K., & Sapate, S. G.. Tribological behaviour of HVOF sprayed WC,12Co, WC,10Co,4Cr and Cr_3C_2–25NiCr coatings. *Tribol Int*. **2017**, 105: 55,68. https://doi.org/10.1016/j.triboint.2016.09.025.
38. Grilec, K., Ćurković, L., Kumić, I., & Baršić, G.. Erosion mechanisms of aluminium nitride ceramics at different impact angles. *Materialwiss Werkst*. **2011**, 42(8): 712,717. https://doi.org/ 10.1002/mawe.201100773.
39. Li, X., Ding, H., Huang, Z., Fang, M., Liu, B., Wu, X., Chen, S. Solid particle erosion,wear behavior of SiC–Si_3N_4 composite ceramic at elevated temperature. *Ceram Int*. **2014**, 40(10): 16201,16207.https://doi.org/10.1016/j.ceramint.2014.07.055.